

Improving Topological Detection of Weather Regimes in climate dynamical systems

Soheil Anbouhi

February 10, 2026

Abstract

Weather regimes provide a useful framework for describing large-scale atmospheric variability and its impacts on regional weather. Despite extensive study, there is still no universally accepted definition or method for identifying weather regimes. Recent work has shown that weather regimes can be interpreted geometrically as topological structures in the phase space of the atmospheric system. In this approach, regimes are identified using a density–radius bifiltration combined with persistent homology, a well-established tool from Topological Data Analysis (TDA). This topological perspective provides a unifying view of regimes and, unlike traditional methods, does not require the number of regimes to be specified in advance. However, the method relies on density estimation techniques (typically Gaussian kernel density estimation), which can over-smooth weakly populated but dynamically important regions of the phase space. Building on this perspective, we introduce a centrality–radius bifiltration that can be tuned to capture both local and global structures in the data. Here, centrality is measured using the k -distance-to-measure function, another tool from TDA, which quantifies the similarity of a state to its k nearest neighbors based on distance information. When combined with persistent homology, this approach improves the topological detection of weather regimes in both idealized dynamical systems and an observational jet latitude dataset. We also incorporate our method into the existing software framework introduced in the original study.

Keywords: weather regimes, atmospheric dynamics, topological data analysis, persistent homology, bifiltration, kernel density estimation, distance-to-measure, centrality measure.

1 Introduction

The atmosphere is a nonlinear, chaotic dynamical system. Yet, its large-scale variability can be described using a few recurrent, quasi-stationary circulation patterns, known as weather regimes. These regimes reflect the atmosphere’s tendency to remain in particular circulation states for extended periods before transitioning to another Legras and Ghil [1985], Vautard [1990], Corti et al. [1999], Hannachi et al. [2017a]. In phase space—where each point represents a possible atmospheric state—weather regimes correspond to regions in which the

system’s trajectory slows, lingers for extended periods (quasi-stationary), and to which it returns repeatedly (recurrent). In the Northern Hemisphere, a familiar case is atmospheric blocking, where a stable high-pressure anomaly disrupts the typical zonal flow for several days. Similarly, large-scale patterns such as the North Atlantic Oscillation (NAO) and the Pacific–North American (PNA) pattern describe recurrent shifts in pressure and circulation that shape weather across broad regions Hannachi et al. [2017b].

The importance of weather regimes lies in their ability to simplify the complexity of atmospheric behavior while improving predictability by linking large-scale circulation patterns to local weather impacts Hannachi et al. [2017b]. Despite decades of research, however, there is still no universally accepted definition or detection method for weather regimes. Traditional approaches—such as clustering techniques, Markov-based models, or self-organizing maps—rely on user-defined parameters, often including or implicitly determining the number of regimes. As a result, applications to Euro-Atlantic circulation have reported between two and seven distinct regimes depending on the method and parameter choices Strommen et al. [2023]. Moreover, many of these approaches become computationally inefficient as the dimensionality of the data increases, reflecting the well-known curse of dimensionality.

Motivated by these challenges, Strommen et al. [2023] proposed a topology-based framework for identifying weather regimes. In this framework, regimes correspond to non-trivial topological structures—such as connected components and loops—within the attractor of the atmospheric system.

To detect these structures, the authors employ persistent homology (PH), a key tool in topological data analysis (TDA) Carlsson [2009]. The basic idea is to construct a nested sequence of subsets of the data, known as a filtration (see Fig. 5). Persistent homology then tracks how topological features persist across the filtration by recording the scale at which each feature appears (“birth”) and disappears (“death”). Each feature is represented as a point with coordinates (birth, death) in the plane. The resulting plot—referred to as the persistence diagram—provides a compact topological summary of the data shape. Features with longer lifespans (death minus birth) typically represent significant structures, whereas short-lived features are less important.

Because climate datasets are typically high-dimensional and densely sampled, some meaningful topological features can disappear when standard persistent homology is applied, making the PH approach less effective for regime identification (see Fig. 8a). To address this issue, Strommen et al. [2023] introduced a density–radius bifiltration method. In this approach, the pointwise density of the dataset is first estimated; for example using Gaussian kernel density estimation (KDE). Then, for a fixed density threshold p , the dataset is filtered to keep only the densest $p\%$ of points, after which PH is applied to extract significant topological features. We can then track how topological features change as we vary p (see Fig. 8b).

This method was tested on three classical dynamical systems and an observational climate dataset that exhibit very different regime behavior. The dynamical systems differ in how dense and how persistent their regimes are, making them a strong test of how the method generalizes. In all cases, the extracted topological features successfully describe the essential regime behavior. Therefore, topology can be considered as a unifying property across these most well-known regime systems. Indeed, Strommen et al. [2023], argued that no single, simple definition of a regime—based solely on density, persistence, or recurrence—can

adequately describe all systems.

Furthermore, their method overcomes several limitations of earlier methods: it does not require the number of regimes to be set in advance and scales efficiently to large, high-dimensional datasets.

A limitation of their method is that, in some cases, the choice of density estimator can significantly influence regime identification. In Strommen et al. [2023], two estimators are considered: Gaussian KDE and direct binning method (histogramming). KDE can be viewed as a smooth, continuous analogue of direct binning. Both methods require careful tuning of parameters (the bandwidth in KDE or the number of bins in direct binning) to avoid under-smoothing noise or over-smoothing meaningful structure. Although automatic bandwidth-selection rules such as Scott’s rule exist for KDE, the resulting Gaussian KDE-based bifiltration may still over-smooth small-scale yet dynamically significant features.

This limitation is evident in the JetLat dataset (Section 5.4), where the jet latitude index exhibits a trimodal distribution corresponding to southern, central, and northern jet positions. The southern jet regime, however, is not well separated and therefore fails to appear as a distinct connected component in the KDE-based bifiltration (see Section 5.4).

A similar issue arises in the Charney–DeVore system (Section 5.3). Its attractor exhibits two regimes, one of which contains a set of low-density loops that spiral outward in phase space and are clearly visible by eye (see Fig. 9). The Gaussian KDE tends to smooth over these thin structures and, as a result, the topological method fails to detect them. While the direct binning approach improves the detection of these features, it remains less reliable, being highly sensitive to bin size, bin alignment, and data dimensionality Scott [1992], Silverman [1986a].

To overcome these limitations, we replace density with a measure of local centrality in the bifiltration framework. Instead of estimating density directly, we quantify how frequently regions of phase space are visited by measuring how strongly each state is connected to its nearby neighbors. This is achieved using *distance-to-measure* functions, which compute the average distance to a point’s k nearest neighbors and are known to be robust to outliers Chazal et al. [2011]. The parameter k controls the scale of locality: smaller values emphasize fine-scale structure, while larger values provide increased robustness to noise.

The proposed centrality-based bifiltration improves the density–radius bifiltration results for the JetLat dataset by successfully capturing all three jet regimes (southern, central, and northern) across a wide range of k values. For the other datasets considered, the centrality-based approach performs comparably to, or enhances, the topological detection of weather regimes relative to the density-based method. In addition, it is computationally more efficient than the KDE-based bifiltration and, like density-based approaches, scales to large and high-dimensional datasets without requiring the number of regimes to be specified in advance.

The choice of k is data dependent. We therefore discuss how this parameter is selected through experimentation and identify a broad range of locality values for which the centrality-based approach captures both local and global geometric structure (Appendix 6). Finally, we integrate our method into the existing analysis software and provide documentation and examples for broader use.

1.1 Outline

The structure of this paper closely follows that of Strommen et al. [2023] to facilitate direct comparison, as our approach builds on and modifies their original framework. Section 2 describes the datasets used in this study and briefly reviews their associated weather regimes. Section 3 introduces background on topological data analysis and the bifiltration framework of Strommen et al. [2023], and presents our proposed method. Section 4 details the computational setup, including the calculation of KDE, centrality measures, and persistent homology, as well as the significance tests used to evaluate robustness. Section 5 reports the results and compares them with those of Strommen et al. [2023]. Finally, Section 6 summarizes the main findings, discusses current limitations, and suggests directions for future work.

2 Datasets

We use the same datasets analyzed in Strommen et al. [2023]: three derived from classical toy models of atmospheric circulation and one from reanalysis data. Below, we briefly summarize each dataset and discuss their associated regimes. For a full description of the datasets, we refer the reader to Appendix B of Strommen et al. [2023].

2.1 Lorenz–63 model

The Lorenz–63 system Lorenz [1963] is a three-variable chaotic model originally developed as a simplified representation of atmospheric convection. Its attractor has the well-known “butterfly” shape, often interpreted as two alternating weather regimes analogous to zonal and blocked flow patterns in the atmosphere Palmer [1993], Baines [2008], Molteni and Kucharski [2019], Strommen et al. [2023]. Figure 1 shows the projection of the Lorenz–63 attractor used in this study.

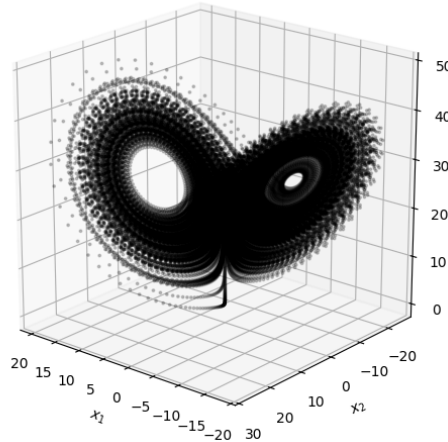


Figure 1: Lorenz–63 attractor simulated with 40,000 data points.

2.2 Lorenz–96 model

The Lorenz–96 model Lorenz [1996] is a simple system designed to mimic chaotic atmospheric dynamics. In the two-scale version used in Lorenz [2006], Christensen et al. [2015], Strommen et al. [2023] and in this study, the model consists of two coupled sets of variables: eight large-scale, low-frequency variables X_k ($k = 1, \dots, 8$), representing dominant modes of variability, and 32 small-scale, high-frequency variables $Y_{j,k}$ ($j = 1, \dots, 32$), representing fast, small-scale processes. This multiscale coupling allows the model to simulate interactions across scales. The regime behavior of the Lorenz–96 system has been discussed extensively Lorenz [2006], Christensen et al. [2015], Strommen et al. [2023]. When the model trajectory is projected onto its leading empirical orthogonal functions (EOFs), the attractor exhibits two regimes: Regime A and Regime B. Regime A corresponds to a high-density region of phase space, and Regime B corresponds to a low-density region separating these dense clusters. In Lorenz [2006], these regimes are described as quasi-stationary flow patterns in which the system lingers near one regime for extended periods before irregularly transitioning to the other. The timing of these transitions is neither periodic nor predictable, reflecting the chaotic nature of the system—analogous to the Lorenz–63 attractor.

Figure 2 shows a three-dimensional projection of the Lorenz–96 attractor onto the first three EOFs used in this study. Even in this low-dimensional view, the looping structure and rotational symmetry characteristic of the Lorenz–96 equations are evident.

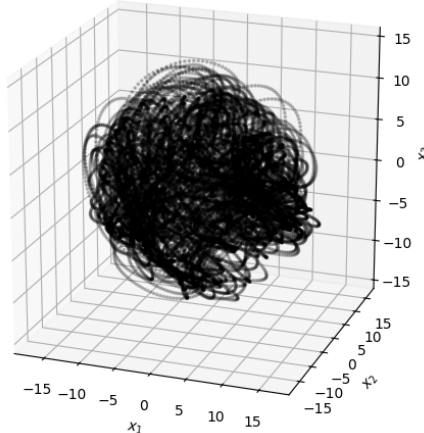


Figure 2: Lorenz–96 attractor projected onto the first three principal components using 40,000 data points.

2.3 Charney–DeVore model

The Charney–DeVore (CdV) model is a simple six-variable system used to study large-scale atmospheric flow Charney and DeVore [1979]. It produces two regimes corresponding to blocked and zonal flow. In the classical view Charney and DeVore [1979], these regimes are related to two fixed points where the model’s trajectory slows down. The fixed point for the blocked regime lies near the dense central region of the attractor, while the zonal regime is

found near the back left corner Strommen et al. [2023]. The blocked regime is more stable and quasi-stationary, while the zonal regime is more turbulent and chaotic Pomeau and Manneville [1980]. In the phase space, the blocking state forms a dense, connected region, whereas the zonal state appears as many low-density loops spiraling outward across a wider area Strommen et al. [2023]. These loops can be seen in raw data (see Fig. 3).

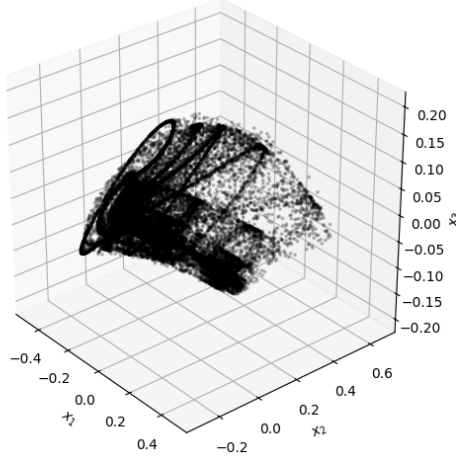


Figure 3: CdV attractor projected onto the first three principal components (40,000 data points).

2.4 North Atlantic jet

The final dataset is observational: the North Atlantic winter jet dataset, known as **JetLat**.

In observations, weather regimes are typically identified from fields that describe large-scale circulation, such as 500 hPa geopotential height or zonal wind. After removing the seasonal cycle, anomalies are projected onto a lower-dimensional space using empirical orthogonal functions (EOFs). The resulting coordinates in this space form a point cloud, from which regimes are detected using clustering or density-based methods Vautard [1990], Michelangeli et al. [1995], Cassou [2008], Hannachi et al. [2017a].

The **JetLat** dataset is derived from the ERA20C reanalysis Poli et al. [2016] (1900–2010) and validated against ERA-Interim Dee et al. [2011] (1979–2015). It provides a simple three-dimensional view of North Atlantic jet variability. For each winter day (December–February), it includes (1) the jet latitude index—the latitude of maximum 850 hPa zonal wind—and (2–3) the first two principal components of 850 hPa zonal wind anomalies. Details on how the jet latitude is computed are given in Parker et al. [2019], Strommen [2020].

Following Strommen et al. [2023], in our study, we use the same variables: daily jet latitude and the first two principal components of 850 hPa zonal wind anomalies over the Euro-Atlantic sector (see Fig. 4).

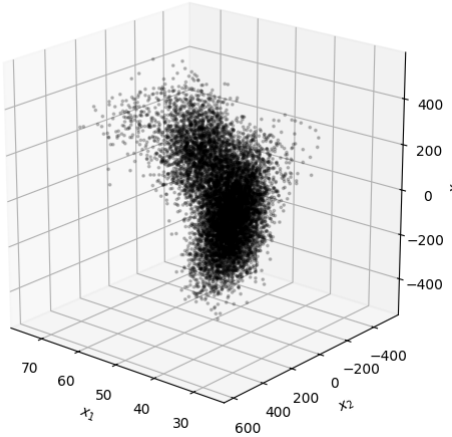


Figure 4: JetLat dataset from reanalysis, comprising about 9,800 data points.

3 Topological Data Analysis

3.1 Persistent Homology

Topological Data Analysis (TDA) is a collection of methods and tools for extracting geometric and topological structure from data. Persistent homology (PH) is one of the most widely used methods in TDA that summarizes topological features (i.e., connected components, loops, voids, etc) across multiple spatial scales in a computationally accessible way.

The first step in PH is to build a nested family of continuous shapes on top of the data. This is done using simple building blocks such as points, edges, triangles, and their higher-dimensional counterparts, called *simplices*. For example, nearby points can be connected at increasing distance thresholds, and whenever a group of points forms a simplex, the region they span is filled in (the Vietoris–Rips filtration). Figure 5 illustrates this process for a noisy sample from a circle.

Persistent homology records when each topological feature appears (its *birth*) and when it disappears (its *death*). Each feature is represented as a point (birth, death) in the plane, encoding its lifespan. The full collection of these points is called the *persistence diagram* of the data. Because a feature must be born before it dies, all points lie on or above the diagonal. Points far from the diagonal correspond to features that persist across many scales and are often interpreted as meaningful structure, whereas points near the diagonal are usually less significant. Figure 6 shows the persistence diagram for the filtration of the noisy circle shown in Figure 5. In this example, all points in the filtration eventually merge into a single connected component (which never disappears), while a prominent loop appears near radius 0.7 and fills in around radius 1.5. These features are visible in the corresponding persistence diagram: the long-lived connected component is shown in blue on the dashed line indicating infinity, and the main loop is represented as (0.7, 1.5) in orange.

For further background on persistent homology, we refer the reader to Chazal et al. [2021], Edelsbrunner et al. [2002], Ghrist [2008], Edelsbrunner and Harer [2010], Otter et al. [2017].

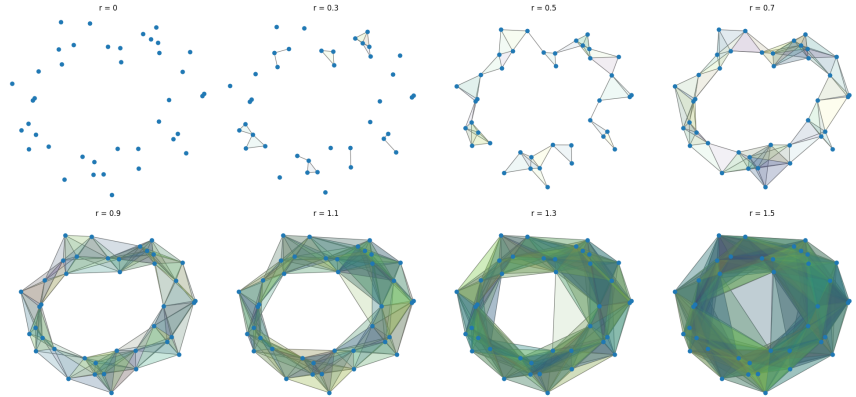


Figure 5: Vietoris–Rips filtration of a noisy circle. For small radius values, edges connect only nearby points, forming small clusters. As the radius grows, these clusters merge and a loop appears. The loop later fills in as the complex becomes fully connected.

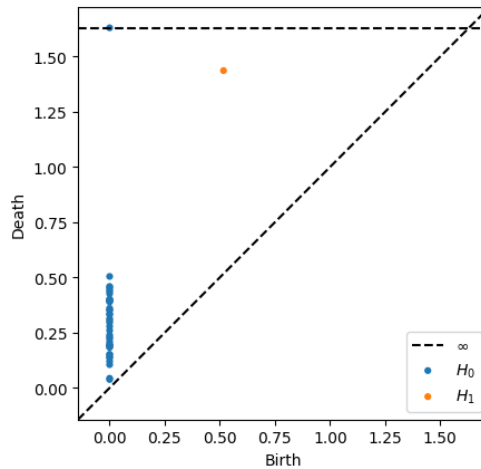


Figure 6: Persistence diagram showing two main topological features from the filtration in Fig. 5: the blue dot on infinity line represents that all points ultimately belong to a single cluster, and the orange dot corresponds to the life span of circular gap that persists through several scales before the circle becomes filled in.

3.2 Bifiltrations for dynamical systems

Standard single-parameter persistent homology may miss important structure in dynamical systems. There are two main reasons for this: (i) many climate-related systems have attractors that are continuous and fully connected Gobbino and Sardella [1997], so a distance-based filtration can recover at most one long-lived connected component; and (ii) some loops in the underlying attractor become harder to detect as the sample size increases. Figure 7 shows how the hole in the right wing of the Lorenz–63 attractor appears to shrink as more points are sampled.

To address this issue, Strommen et al. [2023] introduced a *density–distance bifiltration*. Formally, they first select a density estimator (Gaussian KDE or the direct binning method) to estimate the density at each point of the dataset X .

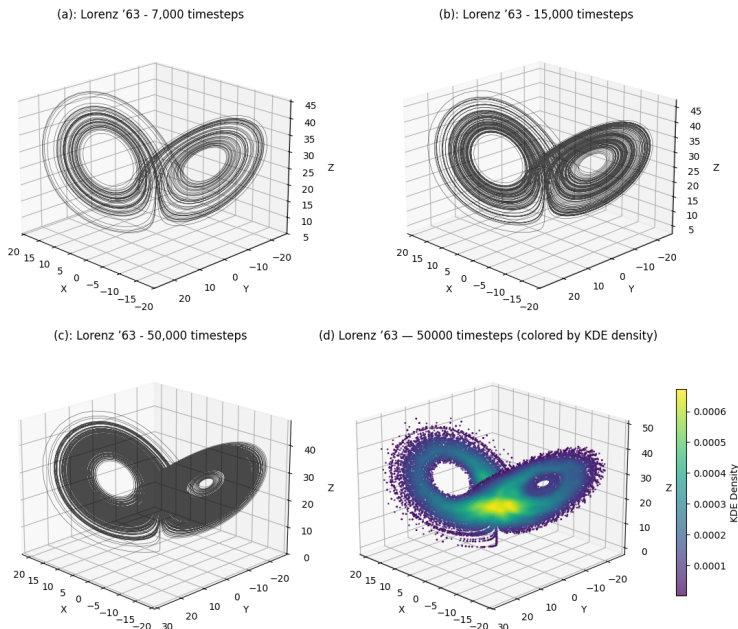
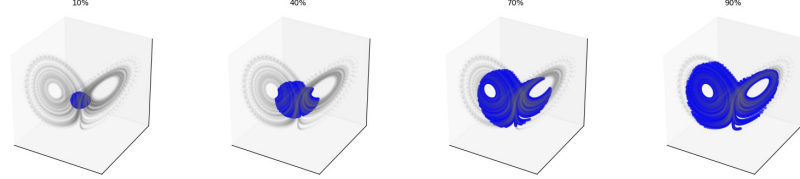


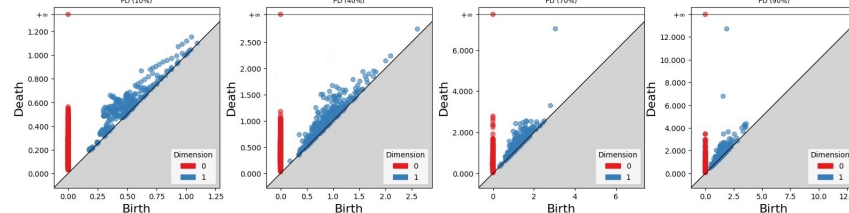
Figure 7: As sample size increases, the smaller loop on the right lobe of the Lorenz–63 attractor shrinks and may not appear in the persistence diagram of a single-parameter filtration. The bottom-right panel shows the full attractor colored by Gaussian KDE to highlight the densest regions.

For a chosen percentile $P \in [0, 100]$, they defined X_P as the densest $P\%$ of points, constructed a Vietoris–Rips filtration on X_P , and applied persistent homology to obtain a persistence diagram for X_P . Varying P produces a two-parameter filtration in which the data are filtered first by density and then by distance. Figure 8 illustrates this process for the Lorenz–63 system.

Then, the top five longest lived features (those that lie well above the diagonal) are extracted and are recorded in a summary diagram that shows how the main topological features persist across different density or centrality thresholds. See Fig. 12d for an example. For further details, see Section 5.



(a) KDE-based bifiltration of the Lorenz–63 attractor.



(b) Persistence diagram corresponding to panel (a).

Figure 8: Density–distance bifiltration of the Lorenz–63 system. Panel (a) shows the Lorenz 63 attractor filtered by density levels (10%, 40%, 70%, 90%), and panel (b) shows the corresponding persistence diagram. At 10% and 40% thresholds, the main feature is a long-lived connected component (red point near $(0, \infty)$). At 70%, besides the long-lived connected component, a significant loop appear which corresponds to the left lobe of the attractor (the farthest blue point from the diagonal). At 90%, two loops are visible, represented by two blue points above the diagonal.

3.3 Limitations of Density-based Bifiltration

Density-based bifiltrations rely on a density estimator which can be insensitive to local, yet dynamically important structures. In Strommen et al. [2023], two density estimation methods are used: a direct binning method and KDE.

Direct binning estimates density by dividing the space into bins and counting the number of data points in each bin. While simple and intuitive, this approach has several well-known limitations. In particular, it is highly sensitive to the choice of bin size and bin alignment, and different choices can lead to different density estimates. More importantly, as the dimension increases, the number of bins grows rapidly while the number of points per bin decreases. This leads to many empty or nearly empty bins and unreliable density estimates, even for large datasets Scott [1992], Silverman [1986a].

KDE is a classical nonparametric method for estimating a probability density function from a finite sample Rosenblatt [1956], Silverman [1986b]. Intuitively, KDE can be viewed as a smoothed version of the direct binning method. Instead of assigning data points to discrete bins, a smooth kernel (typically Gaussian) is centered at each data point. Summing these kernels produces a continuous density estimate. Regions where the kernels overlap strongly, correspond to high density, while isolated regions correspond to low density.

KDE depends on a bandwidth parameter that controls the level of smoothing in the estimated density. If the bandwidth is chosen too large, fine-scale or weakly separated structures may be over-smoothed, while very small bandwidth values tend to amplify noise

Abramson [1982]. For example, in the JetLat dataset, the region corresponding to the southern jet regime is not well separated from the other regimes. When Gaussian KDE is applied, this structure is over-smoothed and consequently is not detected as a distinct connected component in the KDE-based bifiltration (see Fig. 18m–18p). Similarly, thin loops in the CdV dataset are assigned low density by Gaussian KDE; as a result, they are not detected by the density-based bifiltration (see Fig. 9).

3.4 local centrality functions

To better capture fine-scale local structure—such as the southern jet regime in JetLat and the thin loop structures in the CdV system—we introduce a family of continuous functions that quantify centrality of a state in phase space. These functions, termed *local centrality functions*, are derived from the well-known *distance-to-measure* functions Chazal et al. [2011], which measures how strongly each point is connected to its local neighborhood. Given k , the k -distance-to-measure (k -dtm) function d_k finds the k nearest neighbors of each point and computes the average distance to them.

Formally, let $X = \{x_1, \dots, x_n\} \subset \mathbb{R}^d$ be our dataset. The k -dtm is defined by

$$d_k(x) = \left(\frac{1}{k} \sum_{i=1}^k \|x - x_{(i)}\|^2 \right)^{1/2},$$

where $x_{(1)}, \dots, x_{(k)}$ are the k nearest neighbors of x under the Euclidean norm.

The motivation is straightforward: points in dense regions have many close neighbors and therefore take lower dtm values, while points in sparse or weakly connected regions have larger dtm values.

The parameter k controls the scale of structure that is captured: small k values are more sensitive to fine structure and therefore noise. On the other hand, large k values are less sensitive to small variations and emphasize more global topological features. Since

$$d_1 \leq d_2 \leq \dots \leq d_m.$$

increasing k , can gradually control the level of sensitivity from very fine local geometry to the global organization of the data.

The *local centrality function* $C_k(x)$ used in this study is the normalized and inverted form of the dtm:

$$C_k(x) = 1 - \frac{d_k(x) - \min_j d_k(x_j)}{\max_j d_k(x_j) - \min_j d_k(x_j)}.$$

In practice, k is selected empirically. A common starting point is to set k as a small fraction of the dataset size, typically within the range 0.01%–1%. The procedure used to select k for our datasets is described in Appendix 6.

Figure 9 compares the performance of KDE, direct binning and the local centrality functions (C_1 and C_n) on the CdV dataset.

From a computational perspective, the standard KDE approach (as used in Strommen et al. [2023]) is relatively expensive, since it requires comparing every data point with every other to estimate the density. In contrast, the dtm-based centrality method estimates local

structure using nearest-neighbor searches, which are generally faster to compute for large datasets. A more detailed discussion comparing dtm and KDE is provided in Appendix 6.

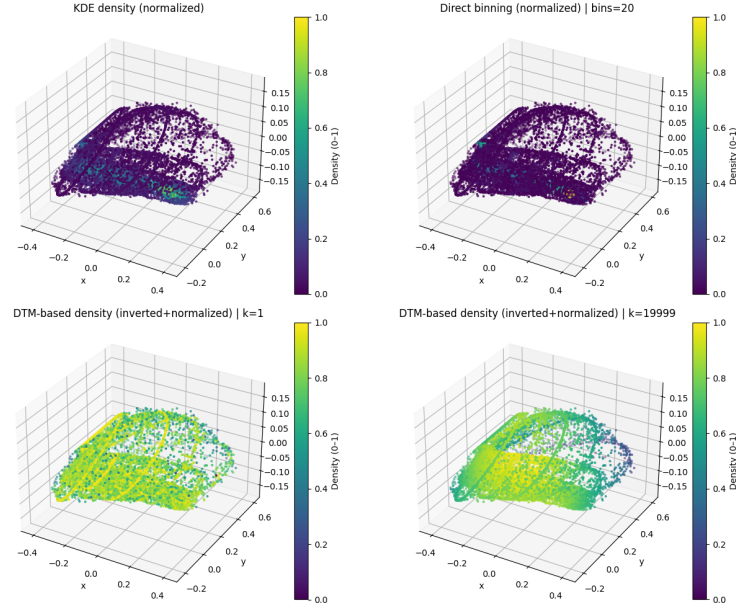


Figure 9: Comparison of KDE, direct binning, and centrality-based methods for the CdV system with 20,000 data points. Top-left: Gaussian KDE highlights the dense central region while assigning low values to the thin loop structures. Top-right: direct binning with 20 bins per coordinate, highlighting mainly the central region. Bottom-left: C_1 and bottom-right: C_{19999} assign high values to both the central region and loop structures, with C_1 placing stronger emphasis on the loops.

4 Computational Methodology

We begin with a dataset. Each state is treated as a point in a multidimensional space. Our computational approach follows Strommen et al. [2023] with several extensions. It includes five main steps, summarized below, with details given in the following subsections.

1. **Normalization.** Each coordinate of the data set is normalized to have unit variance. The resulting data set is denoted by X .
2. **Evaluation of KDE or Centrality** A scalar function is chosen—either Gaussian KDE, binning, or centrality with k neighbors C_k —and its value is computed at each data point.
3. **Density or centrality thresholding.**

A filtration is constructed by selecting a sequence of percentiles $p_1 < p_2 < \dots < p_l$. For each percentile p_i , we form a subsample X_{p_i} containing the top p_i -percent of

points—those with the highest KDE densities or, when using centrality, the highest centrality values.

4. **Persistent homology** is then computed on each X_{p_i} using the `Gudhi` library. From each persistence diagram, birth and death times, and the longest-lived connected components are extracted. We also use `Persloop` to compute representative cycles of the longest-lived loops. For visual simplicity, only the five longest-lived features are considered; for the data considered here, no essential information is lost by this restriction Straus et al. [2007], Strommen et al. [2023].
5. **Bifiltration.** Steps (2)–(4) are repeated for $P = 10\%, 20\%, \dots, 100\%$, producing a family of subsamples filtered by either density or centrality. These thresholds are sufficient for the datasets used here, though finer thresholds may be helpful for more complex dynamics.

Further details on the main computational steps are given below.

4.1 KDE and Local Centrality Functions

Local densities are estimated using `scipy.stats.gaussian_kde` with Scott’s rule for automatic bandwidth selection.

The distance-to-measure function d_k is computed by finding the k nearest neighbors of each point (excluding the point itself) using `scikit-learn`’s `NearestNeighbors`, and taking the root-mean-square (RMS) distance to these neighbors. To compute the centrality function C_k , we apply min–max normalization and invert the values.

The value of k is chosen empirically. A discussion on how we select k for each dataset is given in Appendix 6.

4.2 Computation of Persistent Homology

Persistent homology is computed using the Vietoris–Rips complex with the Python package `Gudhi`. We calculate only dimensions 0 (connected components) and 1 (loops). The main parameters and their settings follow those used by Strommen et al. [2023] and are summarized below.

- **max_edge:** the largest distance allowed when connecting points to build the Vietoris–Rips complex. Without this parameter, every pair of points is a potential edge, and the number of simplices grows exponentially. We set `max_edge = 5.0` for all datasets.
- **min_pers:** sets a minimum persistence threshold, removing short-lived topological features that are typically unstable and noise-induced. Values between 0.15 and 0.50 are used, with larger values for datasets with fine structures such as CdV.
- **sparse:** reduces the number of connections to make the computation faster while keeping the main structure. We use `sparse = 0.7` for all datasets, keeping about 70% of the links.

- `pre_sparse`: this parameter applies a preliminary sparsification to the point cloud using `gudhi.sparsify_point_set`, removing a small fraction of points while maintaining the overall topology. This step helps reduce computation time, especially for large datasets. We use 0.05 for Lorenz-63 and Lorenz-96, 0.005 for CdV to preserve finer detail, and no sparsification for JetLat, which already contains fewer points.

4.3 Representative Connected Components and Loops

We use the implementation provided by Strommen et al. [2023] to compute connected components and representative loops. Connected components are extracted directly from the `Gudhi` filtration, while representative loops are computed using `PersLoop` Dey et al. [2018]. As mentioned before, we focus on the five longest-lived connected components and 1-cycles identified in the persistence diagrams.

4.4 Significance Testing and Reliability of Topological Features

Not all topological features in a persistence diagram correspond to meaningful structure in the data. Some may arise from noise, random sampling, or parameter choices. To identify reliable features, we adopted the significance tests of Strommen et al. [2023] and extended them to our centrality-based framework.

(1) Sensitivity tests for persistent homology. We repeated the analysis using different filtering thresholds and homology settings. The overall shape of the persistence diagrams and the position of the major connected components remained consistent across runs, indicating that these features are stable. Loop features showed more variability and are therefore interpreted as qualitative indicators of the attractor’s geometry rather than precise structural elements.

(2) Gaussian reference test. To estimate the level of topological noise expected from an unstructured distribution, we generated 10,000 random points from a three-dimensional Gaussian distribution with unit variance. Both method—the KDE-radius and the centrality-radius bifiltrations—were applied. For each random sample and each filtration, we recorded the *maximum* lifespan observed for connected components and loops. The experiment was repeated ten times. The largest lifespan observed (no greater than 0.5) was used as the noise threshold; features with lifespans exceeding this value were considered non-trivial.

5 Results

Following the implementation of Strommen et al. [2023], we summarize the structure of each dataset using *bifiltration diagrams*. These diagrams encode how significant connected components and loops appear and persist as the filtration threshold (density or centrality) varies. The horizontal axis represents the filtration threshold, while the vertical axis indicates the lifespan of each feature. At each threshold, the five longest-lived connected components and loops are displayed. The dashed line shows the maximum lifespan obtained from the Gaussian reference test, which serves as a baseline for identifying topological noise.

The `min-pers` line marks the smallest lifespan required for a feature to be considered significant.

To further distinguish significant clusters, we also include a color and shape code based on the size of connected components: small components with fewer than four points are treated as noise (red “ \times ”), components with four to ten points are classified as weak features (yellow diamonds), and components with more than ten points are considered robust (red circles). Note that these thresholds can be adjusted by users. Loop features are shown as blue triangles, following the convention of Strommen et al. [2023]. Fig. 10 shows a centrality-based bifiltration diagram for a random sample generated from three-dimensional Gaussian distribution.

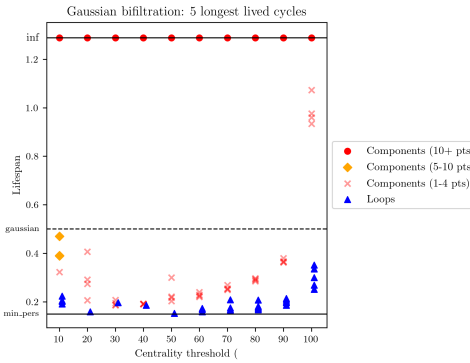


Figure 10: Persistence summary across centrality thresholds for the Gaussian reference test.

5.1 Results for the Lorenz–63 System

Recall that the Lorenz–63 attractor resembles a “butterfly” shape, with each wing commonly interpreted as a distinct regime. In the bifiltration framework, these regimes correspond to two loops in the topological representation. Both the KDE-based and centrality-based methods (across all (k)) recover the well-known these topological loops. However, the centrality method, for smaller k values ($k \leq 100$) identifies them earlier in centrality thresholds. That means, these topological features persist across more centrality threshold, and therefore more significant (see Fig. 11).

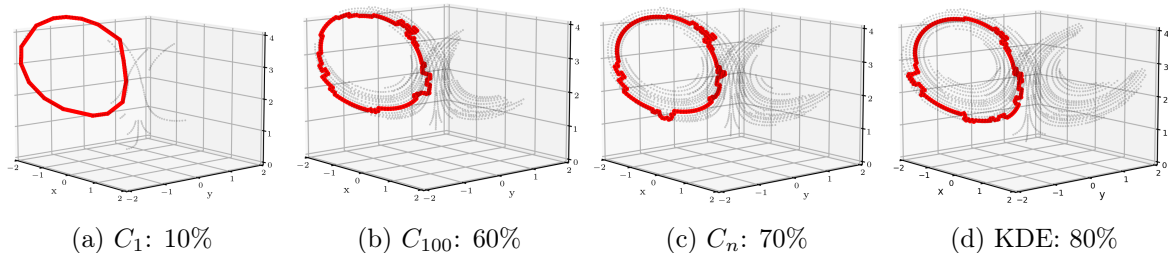


Figure 11: Lorenz–63: the first persistent loop (left lobe) identified by both methods. Panel 11c shows C_n with full neighborhood size.

For larger k values, the behavior of the centrality method becomes increasingly similar to that of the KDE-based approach. This pattern is illustrated in Fig. 12.

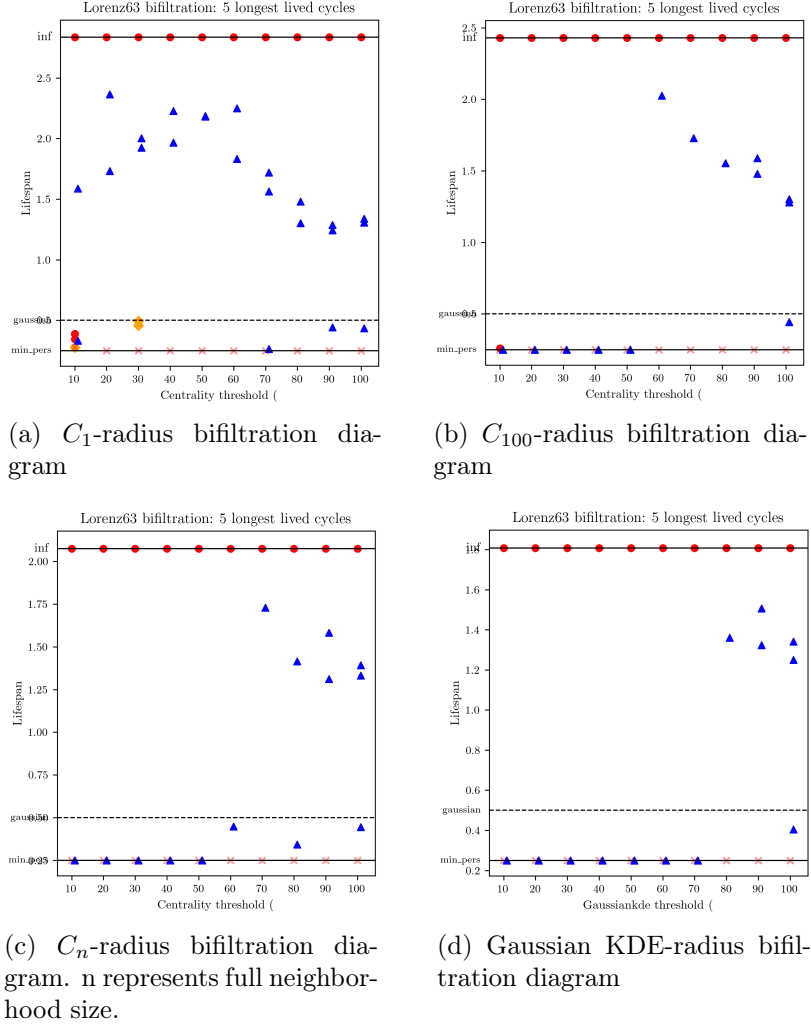


Figure 12: Lorenz-63: comparison of centrality-based and KDE-based method. Centrality functions generally detect the topological loops earlier compare to KDE-based method.

5.2 Results for the Lorenz-96 System

Recall that the Lorenz-96 system has two main regimes, referred to as Regime A and Regime B. In phase space, Regime A corresponds to a high-density region forming a large loop along the outer edge of the attractor, while Regime B corresponds to a lower-density region near the center. Both KDE and centrality-based methods successfully identify the dominant regime-related structures in phase space. As in the Lorenz-63 case, the centrality-based method with smaller k values captures these structures at lower centrality thresholds. Larger k values, on the other hand, smooth out fine details and behave similarly to the Gaussian KDE-based method. In all cases, the bifiltration first detects the densest parts of the

attractor as several connected components. As the threshold increases, these components merge and the looping structures emerge. This looping behavior of the system, can be also observed in Fig. 2.

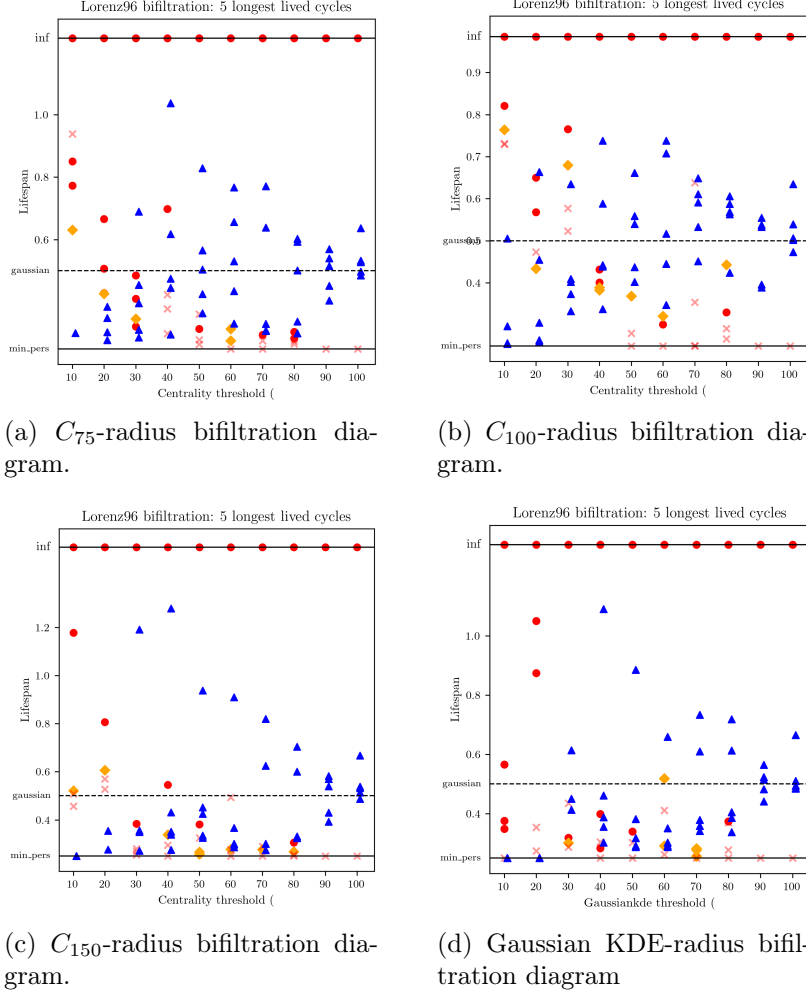


Figure 13: Lorenz-96: comparison of centrality-based and KDE-based radius bifiltrations. Increasing the locality scale in the centrality functions (C_{75} , C_{100} , C_{150}) progressively suppresses fine-scale loop structures, leading to behavior that approaches the KDE-based bifiltration.

5.3 Results for the Charney–DeVore System

Recall that the CdV system has two regimes corresponding to blocking and zonal states. In phase space, the blocking regime forms a dense, connected region, while the zonal regime appears as several thin, low-density loops that extend over a wider area.

The centrality method improves the detection of regime-related topological structures in the CdV system. As shown in Fig. 9, Gaussian KDE assigns low values to the thin loops, effectively removing them during the bifiltration process. This behavior is reflected in the KDE-based bifiltration diagram shown in Fig. 14c. In Strommen et al. [2023], a

direct-binning approach is used as an alternative to KDE. The direct-binning method better recovers fine-scale loop structures associated with the zonal regime. For example, as shown in Fig. 14d, the direct-binning method identifies the first loop using about 40% of the data points, with the longest-lived loop having a lifespan of approximately 1.5.

The centrality-based method, on the other hand, identifies regime-related features earlier in the filtration, and the main loops it detects have longer lifespans than those obtained using the binning method. A longer lifespan indicates that the detected feature is more persistent (with respect to distance parameter) and therefore more reliable. Fig. 14 compares bifiltration diagrams from centrality-, KDE-, and binning-based methods. Fig. 15 illustrate the detection of the first persistent loops under these bifiltrations.

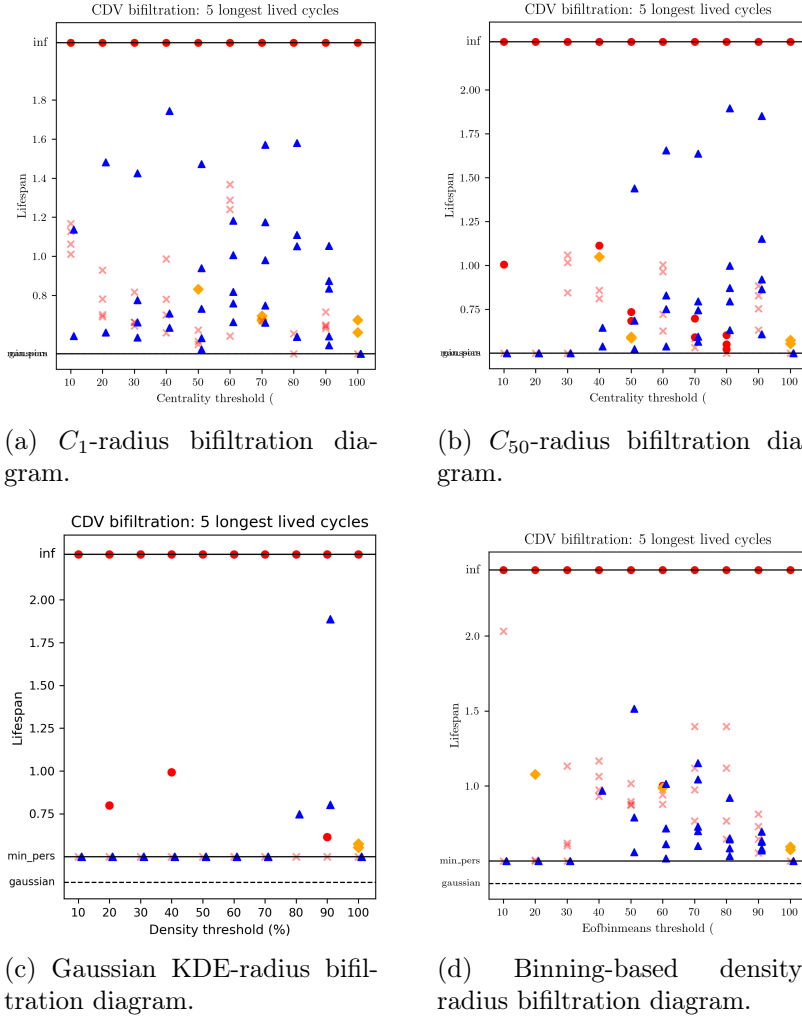


Figure 14: Charney–DeVore: comparison of centrality-based, density-based (KDE), and binning-based bifiltrations. The centrality-based method identifies thin loop structures associated with the zonal regime earlier in the filtration and yields longer-lived, more persistent features than the density- or binning-based approaches

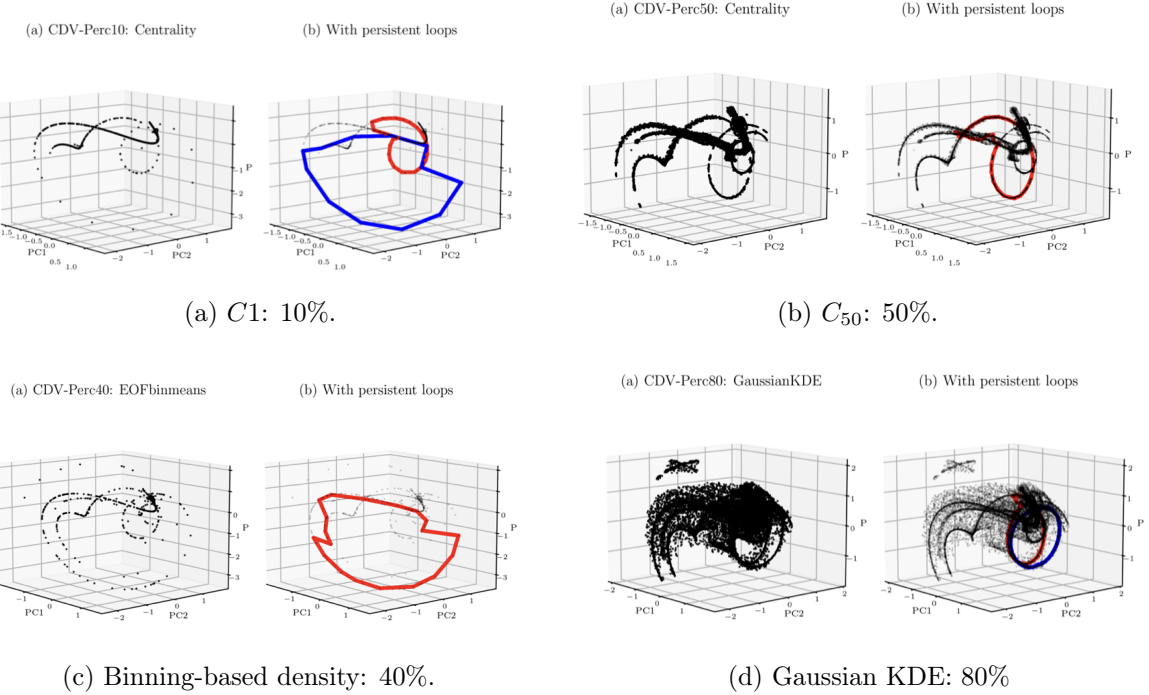
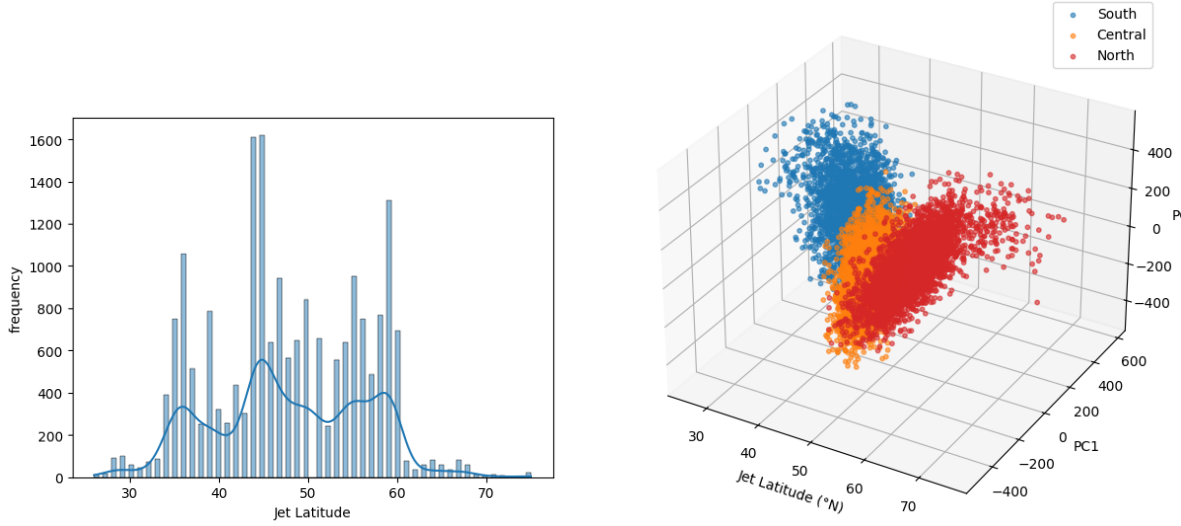


Figure 15: CdV dataset: first persistent loops detected by different bifiltration methods. The C_1 -based method detects two persistent loops at a 10% threshold (Panel 15a), while the C_{50} -based method detects the first loop at 50% (Panel 15b). The binning-based density method identifies the first loop at 40% (Panel 15c), whereas the Gaussian KDE-based method does so only at 80% (Panel 15d). Colors are assigned by `persloop` and indicate loop persistence, with red denoting the longest-lived loop.

5.4 Results for the JetLat Dataset

Recall that the JetLat dataset is three-dimensional and consists of the daily jet latitude index together with the first and second principal components (PC1 and PC2) of 850 hPa zonal wind anomalies. The jet latitude index is known to exhibit a trimodal distribution, reflecting preferred southern, central, and northern jet positions that are commonly interpreted as distinct jet regimes. These regimes are typically defined by clustering the daily jet latitude values [Woollings et al., 2010, Hannachi et al., 2017a, Strommen et al., 2023]. The southern (low jet latitudes), central (intermediate jet latitudes), and northern (high jet latitudes) regimes correspond to the negative, neutral, and positive phases of the NAO, respectively [Woollings et al., 2010, Strommen, 2020]. Figure 16 shows the configuration of these regimes in the JetLat dataset. Regime boundaries are defined by the local minima of the empirical jet-latitude distribution, which separate preferred jet positions.

When applying a Gaussian KDE-based bifiltration, the method fails to recover all three jet regimes. It identifies only two connected components at the 10% density threshold, corresponding to the central and northern jet regimes, while the southern regime is not sufficiently separated to be detected (see Fig. 17d). As noted by Strommen et al. [2023], refining the density threshold or increasing the number of EOFs does not improve this result,



(a) Distribution of jet latitude values in the JetLat dataset.

(b) Organization of Southern, Central, and Northern jet regimes.

Figure 16: Jet latitude distribution and regime organization in the JetLat dataset. Regime assignment is based on local minima in the jet latitude distribution.

suggesting that the two-regime pattern is a robust feature of the KDE-based approach.

In contrast, the centrality-based method exhibits a richer structure. For all tested values of k , it consistently identifies two connected components across low centrality thresholds (typically $p \leq 40\%$). For intermediate neighborhood sizes ($30 \leq k \leq 100$), three to four connected components emerge, and outside of this range the number of connected components again collapses to two (Fig. 17).

To understand the nature of the identified components, we assign regimes based on the dominant jet-latitude proportion within each component, and define purity as the fraction of points belonging to the assigned regime. Table 1 summarizes the results of this procedure for $k = 40$.

p (%)	component size	assigned regime	purity	regime counts (S, C, N)
10	287	North	0.951	(2, 12, 273)
10	676	Central	0.964	(10, 652, 14)
10	13	South	0.769	(10, 3, 0)
20	1902	Central	0.640	(26, 1217, 659)
20	20	South	0.700	(14, 6, 0)
20	12	South	1.000	(12, 0, 0)
20	19	South	1.000	(19, 0, 0)

Table 1: Regime assignment for connected components identified by C_{40} -radius bifiltration.

We note that some connected components correspond to a single weather regime, while others contain points from multiple regimes, which we refer to as mixed regimes. The appear-

ance of mixed regimes is consistent with previous analyses of North Atlantic jet variability. In particular, Madonna et al. [2017] associates such mixed regimes with split or strongly tilted jets and links them to European and Scandinavian blocking.

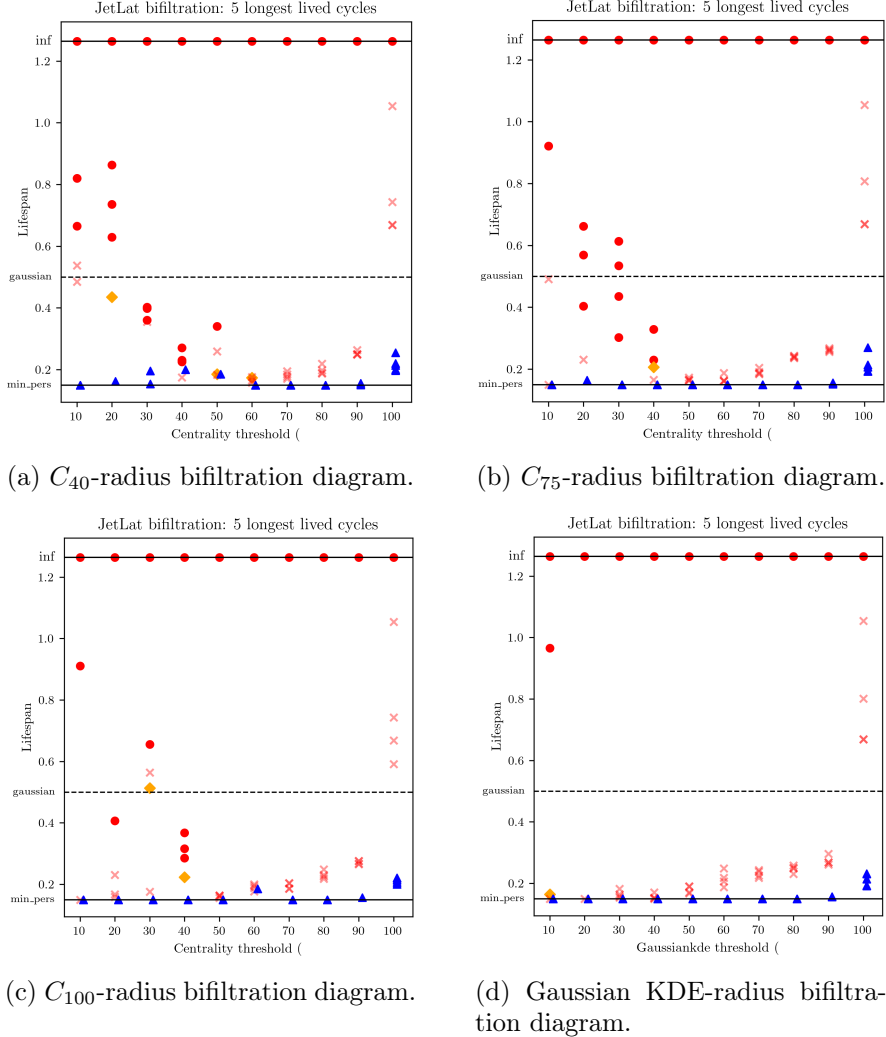


Figure 17: JetLat Dataset: comparison of centrality-based and KDE-based radius bifiltrations. Increasing the locality scale in the centrality functions (C_{40} , C_{75} , C_{100}) progressively suppresses fine-scale regime structure, leading to behavior that approaches the KDE-based bifiltration.

We observed two distinct patterns. First, for $30 \leq k \leq 45$ at $p = 10\%$, three connected components align with the three jet regimes, with the central regime dominant and the southern regime weakest. Second, at $p = 20\%$, the central and northern regimes merge into a single large component, while the southern regime appears as two smaller components (see Figs. 18a–18d). For larger values of k , the behavior is similar to the second pattern: the central and northern regimes are detected at low centrality thresholds, and as the threshold increases, they merge while the southern regime emerges as two components (Figs. 18e–18h).

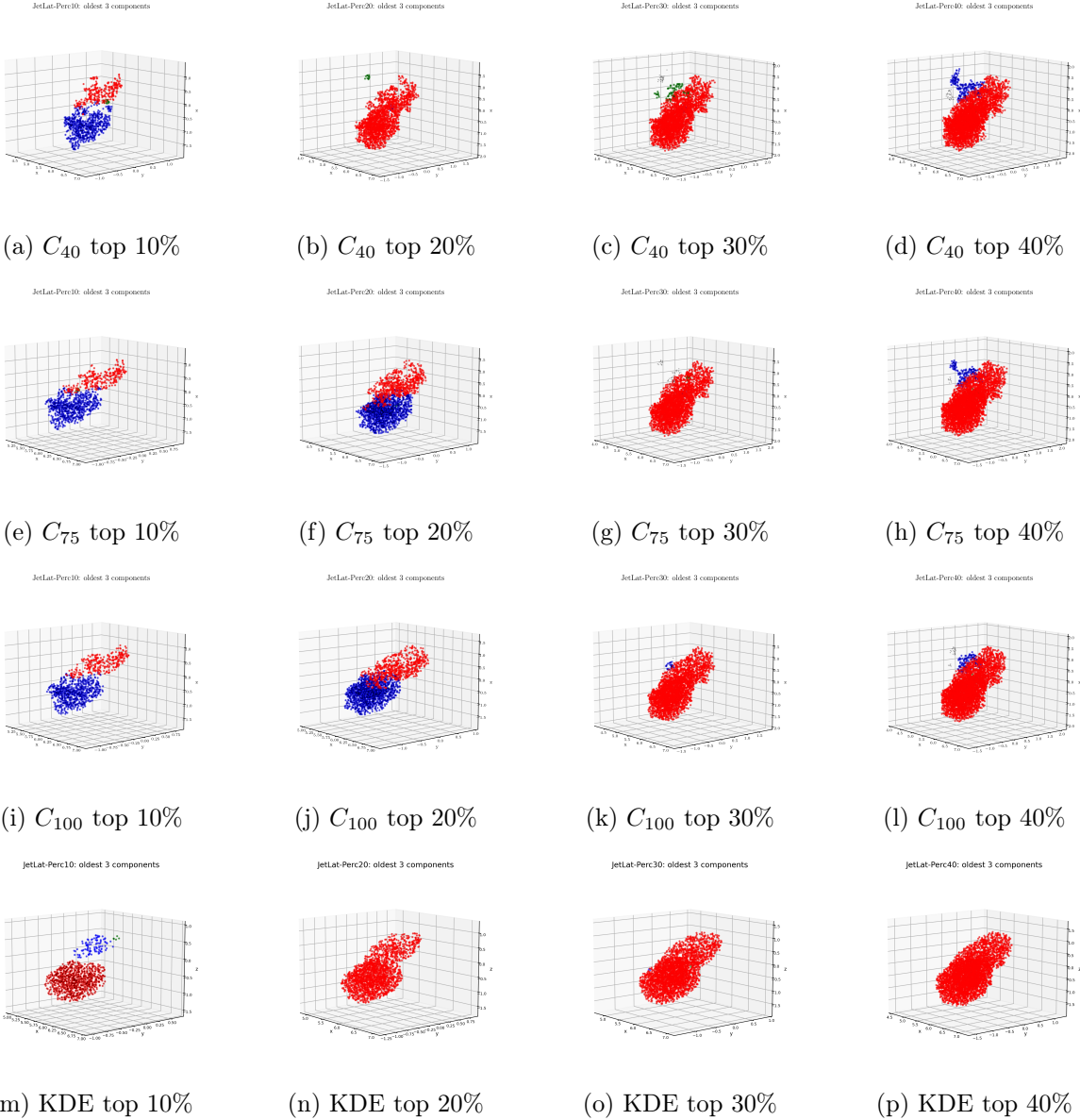


Figure 18: Evolution of connected components in the JetLat dataset across different bifiltration methods and percentile thresholds. Rows correspond to filtering functions (C_{40} , C_{75} , C_{100} , and Gaussian KDE), while columns show increasing percentile thresholds (10%, 20%, 30%, and 40%). Moving from left to right, connected components may emerge or merge, as the filtration progresses. Colors are assigned by `persloop` and indicate relative persistence of connected components, with red denoting the most persistent (longest-lived) component, followed by blue, green, and gray.

6 Discussion, Strengths and Limitations, Future Work

Building on the density-based topological bifiltration framework proposed by Strømmen et al. [2023], this study introduces a centrality-based extension for the topological detection of weather regimes. The original framework relies on a density estimation method (primarily Gaussian KDE), which can miss thin structures and loosely connected clusters. Our approach improves the detection of topological features, enabling clearer identification of meaningful weather regimes across different datasets. In particular, it enhances the detection of thin loop structures in the CdV dataset and successfully identifies the third, weakly separated southern regime in the JetLat dataset, which the original method failed to detect. Beyond these improvements, the centrality-based method is computationally efficient, less sensitive to noise, and straightforward to interpret.

Limitations and Future Work

A primary limitation of the proposed approach is that it does not explicitly incorporate temporal information. As a result, some extracted topological features may reflect purely geometric relationships rather than physically meaningful dynamical behavior. Incorporating temporal or trajectory-based information could help distinguish dynamically relevant regimes, characterize transitions, and ultimately improve the usefulness of the extracted features for forecasting and statistical modeling.

A second limitation concerns the empirical choice of the locality parameter k for noisy datasets. This parameter determines the scale at which local neighborhoods are defined and therefore controls the balance between sensitivity to fine-scale structure and robustness to sampling noise. If k is too small, the method can become overly sensitive to noise, producing fake topological features. If k is too large, weak or short-lived regimes may be smoothed out or merged with dominant ones. Developing a data-driven strategy for selecting k would improve the applicability of the method.

Appendix A: Centrality Functions and the Distance-to-Measure

Let μ be a positive (Borel) probability measure defined on a subset of the Euclidean space \mathbb{R}^d , and let $m_0 > 0$ denote a fixed mass parameter smaller than the total mass of μ . The *distance function to the measure* (dtm) μ with parameter m_0 quantifies how far a point $x \in \mathbb{R}^d$ lies from the bulk of the mass distribution of μ . It is defined as the average distance from x to the smallest Euclidean balls centered at x that contain a proportion $u \leq m_0$ of the total measure. Formally, the dtm function is given by

$$d_{\mu, m_0, r}(x) = \left(\frac{1}{m_0} \int_0^{m_0} \delta_{\mu, u}(x)^r du \right)^{1/r}, \quad (1)$$

where

$$\delta_{\mu, u}(x) = \inf\{t > 0 : \mu(B(x, t)) > u\}. \quad (2)$$

Here, $\delta_{\mu,u}(x)$ represents the radius of the smallest Euclidean ball $B(x,t)$ centered at x that contains a fraction u of the total mass of μ . This measure-theoretic formulation captures the geometric spread of μ around x and provides a smooth, robust alternative to standard distance functions defined over discrete point sets.

For a finite sample $X = \{x_1, \dots, x_n\}$ with uniform probability measure on it, the dtm reduces to its empirical form:

$$d_k(x) = \left(\frac{1}{k} \sum_{i=1}^k \|x - x_{(i)}\|^r \right)^{1/r}, \quad (3)$$

where $k = \lfloor nm_0 \rfloor \in \mathbb{N}$ and $x_{(1)}, \dots, x_{(k)}$ denote the k nearest neighbors of x under the Euclidean metric.

Finally, for consistency with KDE output and interpretability, the dtm is normalized and inverted to define the *local centrality function*

$$C_k(x) = 1 - \frac{d_k(x) - \min_j d_k(x_j)}{\max_j d_k(x_j) - \min_j d_k(x_j)}, \quad (4)$$

so that higher $C_k(x)$ values correspond to points that are geometrically central within their local neighborhoods, while lower values indicate peripheral or transitional regions.

The integer k controls the locality scale of the dtm:

- Small k emphasizes fine, local geometry and is sensitive to filamentary or loop-like features.
- Large k smooths out noise and reflects more global geometric organization.

Since $d_{k_1}(x) \leq d_{k_2}(x)$ for $k_1 < k_2$, increasing k generates a continuous transition between local and global structure, analogous to a scale-space parameter.

In practical applications, k/n acts as a normalized locality fraction; typical values lie in the range 10^{-4} – 10^{-2} depending on sample size.

Here, we summarize key properties of the dtm (Chazal et al. [2011, 2018]):

The function $d_k(x)$ is positive and continuous on \mathbb{R}^d , as it is a mean of continuous nearest-neighbor distances. More importantly, it satisfies a *1-Lipschitz* condition, which guarantees that small changes in x lead to at most equally small changes in the value of $d_k(x)$. Formally, for all $x, y \in \mathbb{R}^d$,

$$|d_k(x) - d_k(y)| \leq \|x - y\|. \quad (5)$$

This property is crucial in practice: it ensures that the dtm varies smoothly over the state space and (depending on the selected k) does not introduce artificial discontinuities even when the underlying data are irregularly sampled or contaminated by observational noise. In the context of atmospheric dynamics, this means that neighboring states in phase space—such as nearby realizations of large-scale circulation patterns—will produce similar centrality values, leading to stable and interpretable topological filtrations.

The choice of the parameter k in centrality functions

The locality parameter k in dtm functions, is typically chosen up to 1% of the total number of data points. We found the same to hold here: for $k > 1\%$, the performance of the centrality method was similar to that of the KDE-based method. For clean and well-sampled datasets, such as our toy models, any value of k within this range worked well, with smaller values revealing regime-related topological structures, earlier in the centrality threshold.

To explore this behavior, we varied k from 1 to 1% of the sample size in increments of 10. For datasets with finer geometric structure, such as the zonal regime in the CdV model and the southern regime in JetLat, smaller step sizes were also tested.

For our toy models, k values up to 50, (approximately 0.1% of the sample size) detected regime-related structures earlier in the centrality threshold, producing subsets that were more representative of the underlying attractor. In particular, for the Charney–DeVore system, we found that thin, low-density loops within this range persisted longer than in the density-based method. For the JetLat dataset, choosing k in the range [0.01%, 1%] of the sample size successfully detects all three main regimes.

Appendix B: Kernel Density Estimation

Kernel density estimation (KDE) provides a smooth, non-parametric approximation of the underlying probability density of a dataset. The idea is simple: at each data point x_i , we place a smooth, bell-shaped kernel function $K(\cdot)$ that spreads its influence over nearby regions of space. Each kernel represents a local contribution to the overall density, centered at x_i and scaled by the bandwidth parameter h .

The final estimate $\hat{f}_h(x)$ is obtained by averaging all these overlapping kernels across the entire dataset (See Fig. 19)

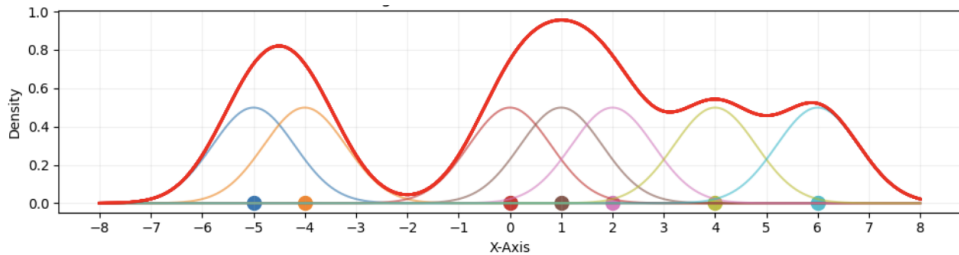


Figure 19: Gaussian KDE. The bandwidth $h = 1$.

Regions where many kernels overlap produce high density values, while regions with few or no kernels yield low density values.

Formally, given $X = \{x_1, \dots, x_n\} \subset \mathbb{R}^d$, the KDE of a probability density f is defined by

$$\hat{f}_h(x) = \frac{1}{nh^d} \sum_{i=1}^n K\left(\frac{x - x_i}{h}\right), \quad (6)$$

where $K : \mathbb{R}^d \rightarrow \mathbb{R}_+$ is a kernel function and $h > 0$ is the *bandwidth parameter*. In this study,

a Gaussian kernel is used:

$$K(u) = \frac{1}{(2\pi)^{d/2}} \exp\left(-\frac{1}{2}\|u\|^2\right). \quad (7)$$

h controls the smoothness:

- Small h reveal fine structures but is sensitive to sampling noise.
- Large h produces a smoother but potentially oversimplified density field.

Automatic choices such as Scott’s rule or Silverman’s rule-of-thumb estimate

$$h_{\text{Scott}} = n^{-1/(d+4)}\sigma, \quad (8)$$

where σ denotes the sample standard deviation. Smaller h values highlight small-scale, low-density features, while larger values merge nearby modes and may obscure distinct weather regimes.

Appendix C: Computational Comparison of KDE and dtm-Based Centrality

From a computational point of view, KDE and the centrality differ in how they scale and how they represent local structure. The standard KDE implementation used in this study (and in Strommen et al. [2023]) computes the Gaussian kernel between all pairs of data points to estimate the local density. This direct approach provides an exact and smooth estimate of the probability density but comes at a high computational cost that scales quadratically with the number of samples, $\mathcal{O}(n^2)$. For large or high-dimensional datasets, this cost quickly becomes restrictive, as every evaluation requires summing the contribution of all other points.

The dtm-based centrality method, by contrast, relies on nearest-neighbor searches rather than pairwise kernel evaluations. Each point’s centrality is estimated by averaging its distances to a fixed number of neighbors, k , typically using tree-based search algorithms such as k -d or ball trees. This procedure scales as $\mathcal{O}(n \log n + nk)$, which is far more efficient when $k \ll n$, and allows the computation to remain tractable for datasets containing tens or even hundreds of thousands of samples. In practice, this efficiency makes the dtm approach two to three orders of magnitude faster than the standard KDE for comparable sample sizes.

Although faster variants of KDE exist—such as tree-based or fast Gauss transform methods that approximate distant kernel contributions and reduce the cost to roughly $\mathcal{O}(n \log n)$ —these methods tend to lose accuracy in high-dimensional settings.

Beyond computational efficiency, the dtm method offers greater robustness and adaptability. Because it is based on distances to neighboring points rather than global kernel overlaps, making it less affected by outliers and uneven sampling.

References

I. S. Abramson. On bandwidth variation in kernel estimates – a square–root law. *Australian and New Zealand Journal of Statistics*, 24(1):21–36, 1982. doi: 10.1111/1467-842X.00283.

Peter G. Baines. Lorenz, en 1963: Deterministic nonperiodic flow. *Progress in Physical Geography: Earth and Environment*, 32(3):355–362, 2008. doi: 10.1177/0309133308091948. URL <https://journals.sagepub.com/doi/10.1177/0309133308091948>.

Gunnar Carlsson. Topology and data. *Bulletin of the American Mathematical Society*, 46(2):255–308, 2009.

Christophe Cassou. Intraseasonal interaction between the madden–julian oscillation and the north atlantic oscillation. *Nature*, 455:523–527, 2008.

Jule G Charney and John G DeVore. Multiple flow equilibria in the atmosphere and blocking. *Journal of the atmospheric sciences*, 36(7):1205–1216, 1979.

Frédéric Chazal, David Cohen-Steiner, and Quentin Mérigot. Geometric inference for probability measures. *Foundations of Computational Mathematics*, 11(6):733–751, 2011.

Frédéric Chazal, Brittany T. Fasy, Fabrizio Lecci, Bertrand Michel, Alessandro Rinaldo, and Larry Wasserman. Robust statistical inference for persistent homology. *Journal of the American Statistical Association*, 113(523):1265–1280, 2018. doi: 10.1080/01621459.2017.1347057.

Frédéric Chazal, Bertrand Michel, Alessandro Rinaldo, and Larry Wasserman. *An Introduction to Topological Data Analysis: Fundamental and Practical Aspects*. Cambridge University Press, Cambridge, UK, 2021.

HM Christensen, IM Moroz, and TN Palmer. Simulating weather regimes: Impact of stochastic and perturbed parameter schemes in a simple atmospheric model. *Climate Dynamics*, 44(7):2195–2214, 2015.

Susanna Corti, Franco Molteni, and TN Palmer. Signature of recent climate change in frequencies of natural atmospheric circulation regimes. *Nature*, 398(6730):799–802, 1999.

Dick P Dee, SM Uppala, Adrian J Simmons, Paul Berrisford, Paul Poli, Shinya Kobayashi, U Andrae, MA Balmaseda, G Balsamo, d P Bauer, et al. The era-interim reanalysis: Configuration and performance of the data assimilation system. *Quarterly Journal of the royal meteorological society*, 137(656):553–597, 2011.

Tamal K. Dey, Tao Hou, and Sayan Mandal. Persistent 1-cycles: Definition, computation, and its application. *Computational Geometry: Theory and Applications*, 67:31–52, 2018. doi: 10.1016/j.comgeo.2018.07.006. URL <https://www.cs.purdue.edu/homes/tamaldey/PersCycle/PersCycle.pdf>.

Herbert Edelsbrunner and John L. Harer. *Computational Topology: An Introduction*. American Mathematical Society, Providence, RI, 2010. ISBN 978-0-8218-4925-5.

Herbert Edelsbrunner, David Letscher, and Afra Zomorodian. Topological persistence and simplification. *Discrete & Computational Geometry*, 28(4):511–533, 2002. doi: 10.1007/s00454-002-2885-2.

Robert Ghrist. Barcodes: the persistent topology of data. *Bulletin of the American Mathematical Society*, 45(1):61–75, 2008. doi: 10.1090/S0273-0979-07-01191-3.

Massimo Gobbino and Mirko Sardella. On the connectedness of attractors for dynamical systems. *journal of differential equations*, 133(1):1–14, 1997.

A. Hannachi, D. M. Straus, C. Franzke, S. Corti, and T. Woollings. Weather regimes: A review of recent research. *Climate Dynamics*, 48(11–12):3157–3172, 2017a.

Abdel Hannachi, David M Straus, Christian LE Franzke, Susanna Corti, and Tim Woollings. Low-frequency nonlinearity and regime behavior in the northern hemisphere extratropical atmosphere. *Reviews of Geophysics*, 55(1):199–234, 2017b.

B Legras and M Ghil. Persistent anomalies, blocking and variations in atmospheric predictability. *Journal of Atmospheric Sciences*, 42(5):433–471, 1985.

Edward N Lorenz. Predictability: A problem partly solved. In *Proc. Seminar on predictability*, volume 1, pages 1–18. Reading, 1996.

Edward N Lorenz. Regimes in simple systems. *Journal of the atmospheric sciences*, 63(8):2056–2073, 2006.

EN Lorenz. Deterministic non-periodic flow. *j. atoms sci.*, 20: 130-141, 1963.

Erica Madonna, Camille Li, Christian M Grams, and Tim Woollings. The link between eddy-driven jet variability and weather regimes in the north atlantic-european sector. *Quarterly Journal of the Royal Meteorological Society*, 143(708):2960–2972, 2017.

P. A. Michelangeli, R. Vautard, and B. Legras. A method for regimelike variations in atmospheric circulation. *Journal of the Atmospheric Sciences*, 52(8):1237–1256, 1995.

Franco Molteni and Fred Kucharski. A heuristic dynamical model of the north atlantic oscillation with a lorenz-type chaotic attractor. *Climate Dynamics*, 52(11–12):6483–6497, 2019. doi: 10.1007/s00382-018-4509-4. URL <https://link.springer.com/article/10.1007/s00382-018-4509-4>.

Nina Otter, Mason A. Porter, Ulrike Tillmann, Peter Grindrod, and Heather A. Harrington. A roadmap for the computation of persistent homology. *EPJ Data Science*, 6:17, 2017. doi: 10.1140/epjds/s13688-017-0109-5.

T. N. Palmer. Extended-range atmospheric prediction and the lorenz model. *Bulletin of the American Meteorological Society*, 74(1):49–65, 1993. doi: 10.1175/1520-0477(1993)074<0049:ERAPAT>2.0.CO;2. URL https://journals.ametsoc.org/view/journals/bams/74/1/1520-0477_1993_074_0049_erapat_2_0_co_2.xml.

Tess Parker, Tim Woollings, Antje Weisheimer, Chris O'Reilly, Laura Baker, and Len Shafrey. Seasonal predictability of the winter north atlantic oscillation from a jet stream perspective. *Geophysical Research Letters*, 46(16):10159–10167, 2019.

Paul Poli, Hans Hersbach, Dick P Dee, Paul Berrisford, Adrian J Simmons, Frédéric Vitart, Patrick Laloyaux, David GH Tan, Carole Peubey, Jean-Noël Thépaut, et al. Era-20c: An atmospheric reanalysis of the twentieth century. *Journal of Climate*, 29(11):4083–4097, 2016.

Yves Pomeau and Paul Manneville. Intermittent transition to turbulence in dissipative dynamical systems. *Communications in Mathematical Physics*, 74(2):189–197, 1980.

Murray Rosenblatt. Remarks on some nonparametric estimates of a density function. *Annals of Mathematical Statistics*, 27(3):832–837, 1956.

David W. Scott. *Multivariate Density Estimation: Theory, Practice, and Visualization*. Wiley, New York, 1992.

B. W. Silverman. *Density Estimation for Statistics and Data Analysis*. Chapman and Hall, London, 1986a.

B. W. Silverman. *Density Estimation for Statistics and Data Analysis*. Chapman and Hall, London, 1986b.

David M Straus, Susanna Corti, and Franco Molteni. Circulation regimes: Chaotic variability versus sst-forced predictability. *Journal of climate*, 20(10):2251–2272, 2007.

Kristian Strømmen. Jet latitude regimes and the predictability of the north atlantic oscillation. *Quarterly Journal of the Royal Meteorological Society*, 146(730):2368–2391, 2020.

Kristian Strømmen, Matthew Chantry, Joshua Dorrington, and Nina Otter. A topological perspective on weather regimes. *Climate Dynamics*, 60(5):1415–1445, 2023.

Kristian Strømmen, Christian M. Grams, Linus Magnusson, and Daniela I.V. Domeisen. A global view of weather regimes: definitions, occurrence and predictability. *Journal of Climate*, 36(15):4827–4848, 2023. doi: 10.1175/JCLI-D-22-0544.1.

Robert Vautard. Multiple weather regimes over the north atlantic: Analysis of precursors and successors. *Monthly weather review*, 118(10):2056–2081, 1990.

Tim Woollings, Abdel Hannachi, and Brian Hoskins. Variability of the north atlantic eddy-driven jet stream. *Quarterly Journal of the Royal Meteorological Society*, 136(649):856–868, 2010.